Performance Sensitivity Studies on the PIAA Implementation of the High-Contrast Imaging Testbed

Erkin Sidick*, John Z. Lou, Stuart Shaklan, and Marie Levine
Jet Propulsion Laboratory, California Institute of Technology, 4800 Oak Grove Drive, Pasadena, CA, USA 91109

ABSTRACT

We have investigated the dependence of the High Contrast Imaging Testbed (HCIT) Phase Induced Amplitude Apodization (PIAA) coronagraph system performance on the rigid-body perturbations of various optics. The structural design of the optical system as well as the parameters of various optical elements used in the analysis are drawn from those of the PIAA/HCIT system that have been and will be implemented, and the simulation takes into account the surface errors of various optics. In this paper, we report our findings when the input light is a narrowband beam.

Keywords: Coronagraph, high-contrast imaging, PIAA, pupil mapping, exoplanets

1. INTRODUCTION

High-contrast imaging testbed (HCIT) at JPL is Terrestrial Planet Finder (TPF) Coronagraph's primary platform for experimentation [1-2]. It is used to provide laboratory validation of key technologies as well as demonstration of a flight-traceable approach to implementation. One of the HCIT implementations consists of a Phase Induced Amplitude Apodization (PIAA) unit [3] at its front end and a sequential two-deformable mirror (DM) subsystem placed between the mapping optics and a science image plane. The PIAA unit serves as a diffraction control subsystem and is used to apodize a beam, while the DMs function as a wavefront control subsystem and can be set to compensate for imperfections in the fabricated optics, as well as flaws (accidental or purposeful) in the diffraction design. It has been shown that paired sequential DMs (e.g., one at a pupil, and one several meters downstream) can be used to generate wavelength-independent amplitude, and that this greatly relaxes the optical surface requirements compared to a single DM or Michelson-DM arrangement [4-6]. In order to validate the PIAA/HCIT hybrid system's performance through modeling and error budget analysis, we have implemented an optical simulation algorithm. It combines a ray trace, diffraction model, and a broadband wavefront control algorithm that operates directly on coronagraphic images, and is similar to the one currently being used on the HCIT system to actively suppress scattered light via precision control of a deformable mirror. This simulation algorithm uses MACOS (Modeling and Analysis for Controlled Optical Systems) as its analytic tool [7]. Hence it is capable of performing full three-dimensional near-field diffraction analysis on HCIT's optical model. Such a diffraction analysis is required to evaluate HCIT's performance in terms of design tolerances and based on its ultimate metric—the contrast ratio.

We have investigated the dependence of the PIAA/HCIT's contrast performance on the rigid-body perturbations as well as surface (phase) errors of various optics. The structural design of the optical system as well as the parameters of various optical elements used in the analysis are drawn from those of the PIAA/HCIT system that have been and will be implemented. This paper presents results on the effects of optical system errors on the PIAA/HCIT narrow-band contrast performance before and after wavefront correction. The dependence of the broadband contrast performance of the PIAA/HCIT system on RB and phase errors of various optics will be studied and reported elsewhere.

2. OPTICAL SYSTEM AND COMPONENTS

The MACOS optical model realistically mimics the PIAA/HCIT. The centerpiece of the HCIT is a 5x8 foot optical table, on which are installed the coronagraph elements as schematically shown in Figure 1. The whole optical table sits in a thermally controlled vacuum tank evacuated with a scroll pump to well below 1Torr. The tank provides the desired

*Erkin.Sidick@jpl.nasa.gov; Phone 1 818 393-7585; Fax 1 818 393-9471; www.jpl.nasa.gov

environment, including vibration isolation, atmospheric turbulence isolation and sub-Kelvin thermal stability. An artificial starlight is created from the output of an optical bare fiber. Various light sources can be fed into the other end of the fiber outside the vacuum tank, such as a narrow band laser beam or a broadband light source with 20% or more bandwidth. Two aspheric mirrors, PIAA M1 and PIAA M2 form a PIAA unit. If needed, a post-apodizer can be inserted to the location of STOP. The PIAA unit reshapes the uniform beam at the entrance pupil into an apodized beam at the exit pupil. The apodizers only do a small fraction of the work, solving the edge-diffraction problem, while the mapping optics do the bulk of the work. The aperture mask or "STOP" after OAP1, which is conjugate to PIAA M2, defines the system pupil of the HCIT. After the DM2, the collimated light is re-imaged by OAP4 onto the focal plane, F4. If necessary, a simple, hard-edged circular occulting mask can be placed at the focal location of F4 to attenuate the starlight without affecting the light of a planet if present. After OAP4 forms an image from the stellar and planet lights, it is then magnified (M ≈3) by the OPA5-OAP6 pair for proper sampling on the CCD science camera located at the final focal plane. On the testbed, the wavefront control software takes the starlight image captured by the CCD camera as an input, finds a new set of DM control commands from it, then updates the settings of the two DMs with the new set of control commands.

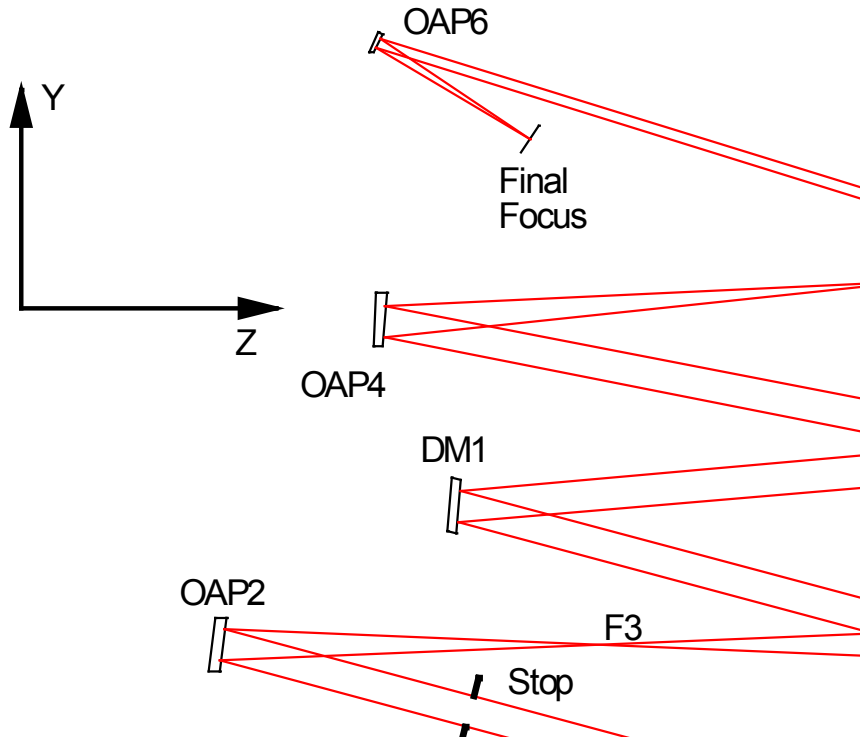

Figure 1. Schematic diagram of the High Contrast Imaging Testbed (HCIT) Phase Induced Amplitude Apodization (PIAA) coronagraph layout. The light source ("starlight") is formed from the output of an optical bare fiber at F1, and a CCD science camera is located at the final focal plane for detecting the image of the "starlight". "OAP" means "Off-Axis Parabolic mirror", M1 and M2 are mirrors, and F1-F4 are focal points.

We use a system aperture diameter D=25.7mm and a narrowband input light having a center wavelength of λ_0=800nm throughout our analysis. The characteristics and the physical parameters of the DMs used in this study are identical to those described in detail in Ref. [1], therefore, they will not be explained here. The illuminating beam of the current system exhibits a small level amplitude-drooping at the exit pupil, but this effect will not be taken into account in this paper. The profile of the apodized beam and the phase errors of the various optics assumed will be described separately in the following sub-sections.

2.1 Apodized Pupil Profile

As mentioned earlier, the PIAA unit consists of two aspheric mirrors, PIAA M1 and PIAA M2, and a pre- and a post-conventional or binary apodizers (not shown), see Fig. 1. It accepts a uniform beam at its input, and delivers an

apodized beam at its output. The output of the PIAA unit can be described by a radially symmetric apodized pupil or a beam surface brightness function: It is a function of distance to the center of the beam. Figure 2(a) shows an example of an apodized pupil profile. This particular apodization function was designed by O. Guyon [8], and will be used in the upcoming simulations of this paper. The inner working angle (IWA) for this profile was estimated to be slightly larger than $2\lambda/D$ on the sky at the $1x10^{-12}$ contrast level. Figure 2(b) shows the corresponding ideal, high contrast PSF.

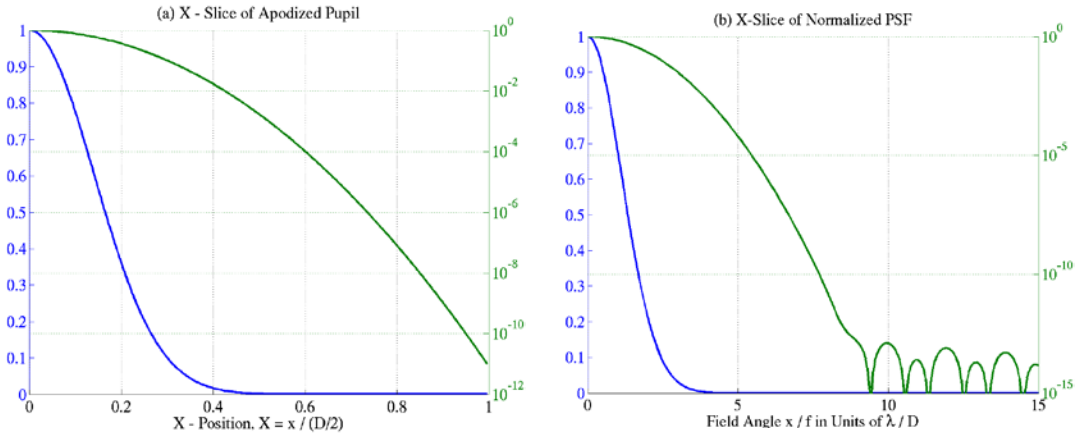

Figure 2. (a) Apodization profile used on the current PIAA/HCIT system and (b) corresponding high contrast PSF.

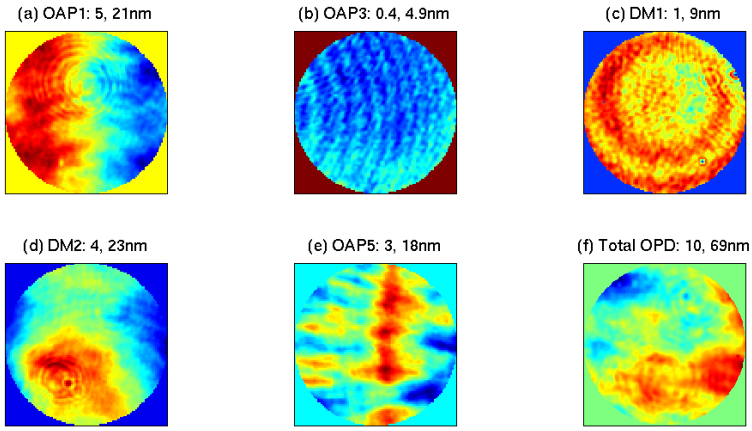

Figure 3. The first five parts, (a)-(e), show the surface height maps used in some of the simulations in this paper, and part (f) is the resulting Optical Path Difference (OPD) exhibited at the exit pupil of the optical system shown in Fig. 1. Also shown in the title of each figure are the root-mean square (RMS) and the peak-to-valley (PV) values of the surface height or OPD map shown in the corresponding figure.

2.2 Surface Errors of Various Optics

No surface height measurement has yet been done on the various optics in Fig. 1. Therefore, we used in our current simulations the surface height data of the HCIT optics measured previously. The measured surface height data were explained in Fig. 4 of Ref. [9]. We use only some of those data as shown in Fig. 3 in this paper, with the purpose of introducing some realistic phase errors into the system to analyze. That is, we introduce the surface error maps shown in the first five parts of Fig. 3 into OAP1, OAP3, DM1, DM2 and OAP5, respectively. The resulted total Optical Path Difference (OPD) at the exit pupil has RMS = 10nm and PV = 69nm, respectively, as shown in Fig. 3(f).

3. ABOUT THE WAVEFRONT CONTROL ALGORITHM

We use the following two wavefront control (WFC) methods in this paper: "Least-square compensator with a tolerance" and "minimum-wavefront and optimal control compensator". These approaches are described in detail in Ref. [10], therefore, will not be explained here. The second approach is also called "Actuator regularization" [11]. The wavefront control algorithms described in Ref. [10] use the wavefront at the system exit pupil as their inputs, and calculate the actuator commands as their outputs. In the present case we set the DM actuators to superpose the negative of the electric field onto the image plane, with a goal to make the image intensity zero on some region Ω on the image plane. Therefore, the WFC algorithm uses an electric field column-vector $\vec{\mathbf{e}}$ as its input, where

$$\vec{\mathbf{e}} = \begin{bmatrix} \Re(\vec{\mathbf{E}}) \\ \Im(\vec{\mathbf{E}}) \end{bmatrix}. \tag{1}$$

For the "minimum-wavefront and optimal control compensator", the joint cost function now becomes as [10]

$$J = \frac{1}{2}\left(\vec{\mathbf{e}}^T\vec{\mathbf{e}} + \gamma_{\text{wu}}\vec{\mathbf{u}}^T\vec{\mathbf{u}}\right), \tag{2}$$

and the gain matrix $\widetilde{\mathbf{G}}$ is obtained from

$$\widetilde{\mathbf{G}} = \left[\left(\widetilde{\mathbf{S}}^T\widetilde{\mathbf{S}}\right)^{-1} + \gamma_{\text{wu}}\widetilde{\mathbf{I}}\right]\widetilde{\mathbf{S}}^T. \tag{3}$$

In Eq. (1), $\vec{\mathbf{E}}$ is the column-vector of the complex electric field on region Ω. It is formed by stacking the elements of the complex electric field on region Ω in the image plane in a certain order, as was explained in Eq. (1) of Ref. [10]. The $\Re(\vec{\mathbf{E}})$ and the $\Im(\vec{\mathbf{E}})$ are the real and the imaginary parts of $\vec{\mathbf{E}}$, respectively. The MACOS simulation tool calculates the complex electric field at the final focal plane directly. Therefore, the electric field conjugation (EFC) algorithm described in Ref. [11] is not needed in our simulation. We chose to use an annular region Ω from $x/f = 8\lambda/D$ to $12\lambda/D$ in the image plane as our control region. For a simulation grid size of 512x512 pixels, this gave an $\vec{\mathbf{e}}$ size of 2880x1 pixels. There are a total of 2048 DM actuators in the current 2-DM system, but we excluded the actuators with zero or very weak influences, thus reducing the number of the actuators used to 1268.

We will keep track of the following three contrast parameters in this paper: (i) C_b, the mean contrast inside a "Big" annular region from $x/f = 9\lambda/D$ to $11\lambda/D$. (ii) C_s, the mean contrast inside a "Small" annular region from $x/f = 8\lambda/D$ to $9\lambda/D$. (iii) C_m, the "Maximum" contrast value inside the annular region from $x/f = 8\lambda/D$ to $9\lambda/D$. The nominal values of these parameters obtained for the error-free optical system in Fig. 1 without conducting any wavefront control are $C_b = 9.4\text{E}-14$, $C_s = 1.5\text{E}-12$, and $C_m = 1.1\text{E}-11$, respectively.

In the next section, we present the results of several wavefront control examples, while summarizing the values of the above three contrast parameters in a table.

4. SIMULATION RESULTS

4.1 Figure Error Control

Our first example is the case in which an annular dark region is created through WFC when the PIAA/HCIT optical system is distorted by the phase errors explained in relation with Fig. 3. The phase errors degrade the contrast C_b from $C_b = 9.4\text{E}-14$ to $C_b = 2.5\text{E}-6$, which can be improved to $C_b = 1.4\text{E}-12$ after a total of 7 WFC iterations. The nominal PSF map as well as those before and after WFC are shown in Figs. 4(a-c). Figures 4(d-f) show the corresponding exit-pupil OPD maps, and Figs. 4(g-h) show the maps of the total DM actuator strokes used to achieve the present contrast results. As we can see from Figs. 4(e-f), the current wavefront correction method does not correct or

minimize the wavefront error of the optical system, but rather re-distributes it. Figure 5(a) shows the various contrast values as a function of the WFC iteration number, and Fig. 5(b) shows the profiles of the PSFs before and after WFC.

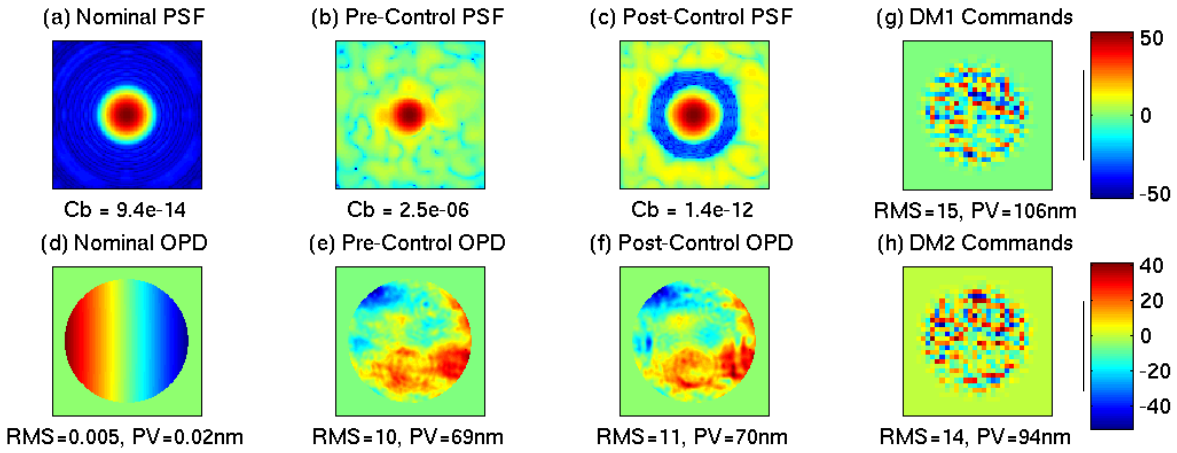

Figure 4. Parts (a)-(c) are the nominal, pre-control and post-control PSF maps plotted in log-scale with a color-map stretch = 1E-15 – 1E0 inside a central $40\lambda/D \times 40\lambda/D$ region, and parts (d)-(f) are the corresponding OPD maps. Parts (g)-(h) show the DM stroke values in nm. The errors included in this simulation are the phase errors shown in Fig. 3

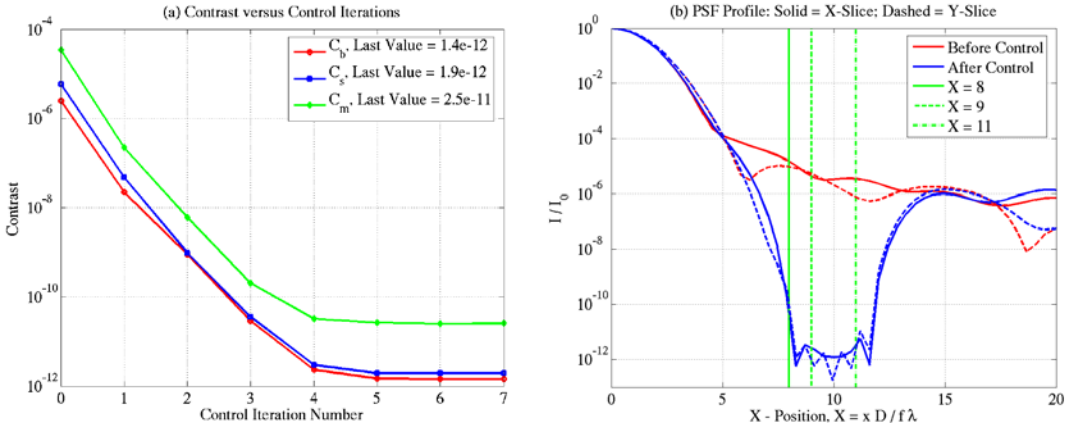

Figure 5. (a) Three types of contrast values versus control iteration number. (b) PSF slices along the x-axis (solid-line) and the y-axis (dashed-line), respectively. In Part (b), $I = I(x, y)$ is the image intensity of the PSF, and I_0 is its peak value. For the Y-Slice of the PSF, the X and the x in the horizontal axis need to be replaced with Y and y, respectively. The errors included in this simulation are the phase errors shown in Fig. 3.

4.2 OAP Rigid-Body (RB) Errors

In general, it is easier to correct the RB errors, such as rotation and xy-translation errors, of an OAP in Fig. 1 using the tip/tilt or the RB actuators (RBAs) of a DM if the DM is so equipped. In such a case, the WFC process needs to be carried out in two steps. The first step is to move the PSF centroid to its nominal position by obtaining the DM x-tilt and y-tilt commands from the shift of the PSF centroid. We call this step as the rigid-body actuator wavefront control or RBA-WFC. In general, this step needs to be carried out only once. The second step is the usual DM actuator (DMA) figure error control, as shown in the previous sub-section. Usually this step needs to be carried out for multiple times. We have tried this approach for a variety of large RB-error scenarios, and found that it is quite effective.

We have also tried a new approach in which we implemented the tip/tilt RBA functionality of DM1 with its DMAs. We call this WFC approach the "Tip/tilt control mode of a DM". The WFC dynamic range of this mode is much smaller as

compared to the RBA-WFC mode of the same DM due to a small stroke range of the DMAs, but it is much easier to implement because it does not require any additional control mechanism in the hardware. This approach is fairly useful when the RB errors of OAPs are not too big. When using this new approach, the WFC process still needs to be carried out in two steps, with the RBA-WFC mode being replaced by the DMA tip/tilt control mode. In this sub-section, we show an example of correcting the x-rotation error of OAP2 with the tip/tilt control mode of DM1 first, followed by the usual DMA figure control step using both DMs. All of the RB errors refer to the global coordinates of Fig. 1 in this paper unless specified otherwise. We chose OAP2 for this analysis because it is located relatively upstream in the optical chain of the current system and thus can serve as a good representative for the understanding on how the PIAA/HCIT system responds to various RB errors.

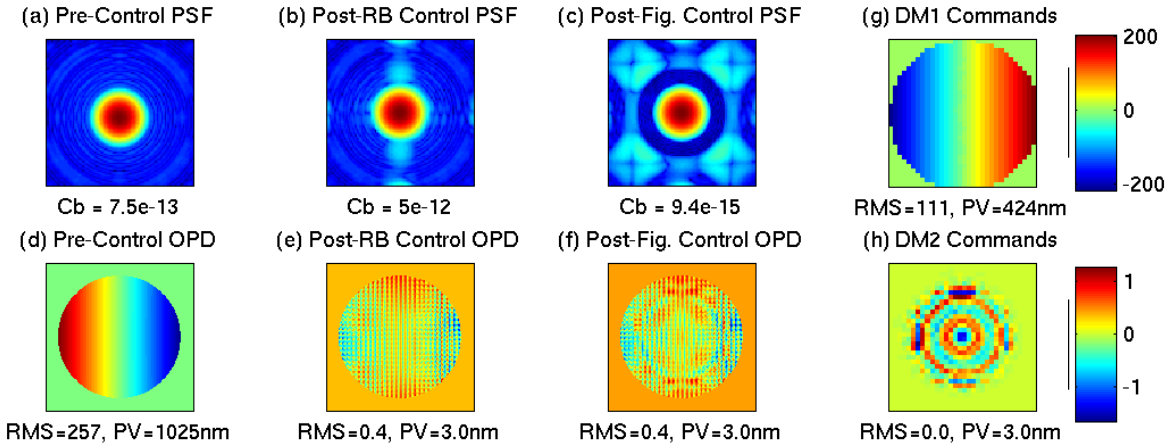

Figure 6. Parts (a)-(c) are the pre-control, post-DMA tip/tilt control and post-DMA figure control PSF maps plotted in log-scale with a color-map stretch = 1E-15 – 1E0 inside the central $40\lambda / D \times 40\lambda / D$ region, and parts (d)-(f) are the corresponding OPD maps. Parts (g)-(h) show the DM stroke values in nm. The error included in this simulation is $R_x = 20\,\mu\text{rad}$ for OAP2. The DMA tip/tilt control step is carried out with DM1 only.

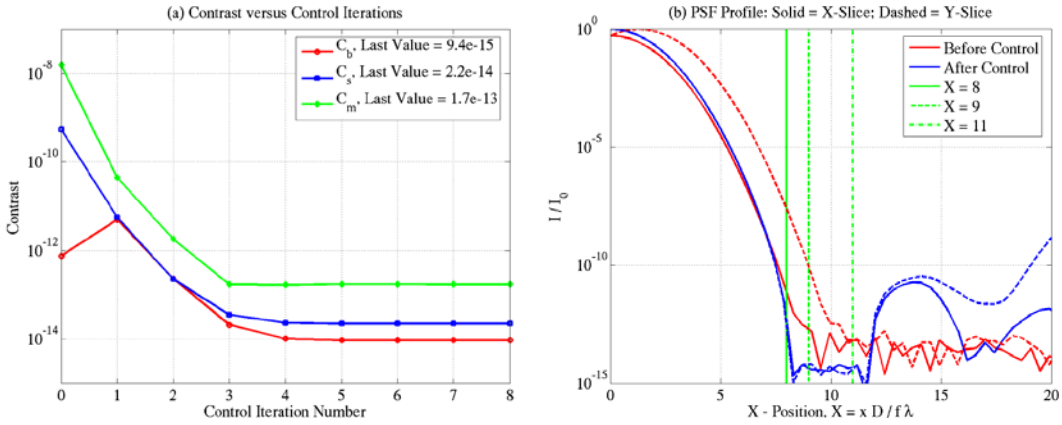

Figure 7. (a) Three types of contrast values versus control iteration number, where Iteration = 1 corresponds to the DMA tip/tilt control step carried out with DM1. (b) PSF slices along the x-axis (solid-line) and the y-axis (dashed-line), respectively. In Part (b), $I = I(x, y)$ is the image intensity of the PSF, and I_0 is its peak value.. For the Y-Slice of the PSF, the X and the x in the horizontal axis need to be replaced with Y and y, respectively. The error included in this simulation $R_x = 20\,\mu\text{rad}$ for OAP2.

Figures 6(a-c) show the PSF maps and Figs. 6(d-f) the corresponding OPD maps at three WFC stages, respectively, when a 20μrad x-rotation error is introduced to OAP2. In this paper, we use R_x, R_y and R_z to denote the angles of

rotation around the x-, y- and z-axes, and T_x, T_y and T_z to denote the distances of translation along the x-, y- and z-axes, respectively. Using this notation, the error introduced in the current case is $R_x = 20\,\mu\text{rad}$ for OAP2. Figures 6(g-h) are the maps of the total DM strokes used. The x-rotation (i.e., a rotation around the x-axis) of OAP2 shifts the PSF from its nominal location, as is seen from the red-curves in Fig. 7(b), and degrades all of the contrast values. Figure 7(a) shows the various contrast values as a function of the WFC iteration number, and Fig. 7(b) shows the profiles of the PSFs before and after WFC.

We have repeated this simulation for the other 5 cases of RB errors of OAP2, and the obtained results are summarized in Table 1 as Cases 4-8. For the case of $T_y = 20\,\mu\text{m}$, the single-iteration DMA tip/tilt control step improves the values of C_s and C_m, but the DMA figure control process, i.e., the second WFC step, does not work. It is not clear whether this problem is caused by the associated physics or by an error in the simulation tool, and this issue is currently being investigated. The three contrast values are fairly insensitive to the z-translation of OAP2, so WFC was not conducted for this case, as is seen by comparing the results of Case 8 with those of Case 1 in Table 1.

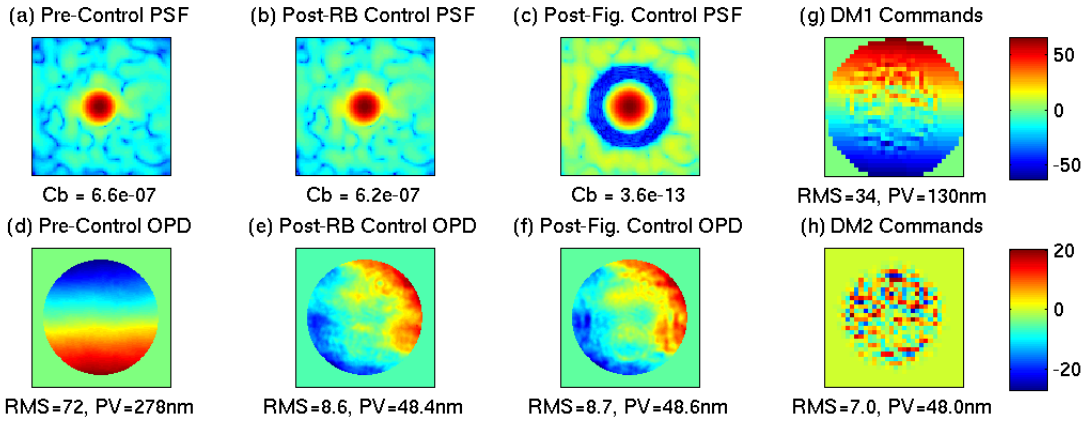

Figure 8. Parts (a)-(c) are the pre-control, post-DMA tip/tilt control and post-DMA figure control PSF maps plotted in log-scale with a color-map stretch = 1E-15 – 1E0 inside the central $40\lambda/D \times 40\lambda/D$ region, and parts (d)-(f) are the corresponding OPD maps. Parts (g)-(h) show the DM stroke values in nm. The errors included in this simulation are the figure errors shown in Fig. 3 divided by 2, plus $R_x = 5\,\mu\text{rad}$ for OAP2. The DMA tip/tilt control step is carried out with DM1 only.

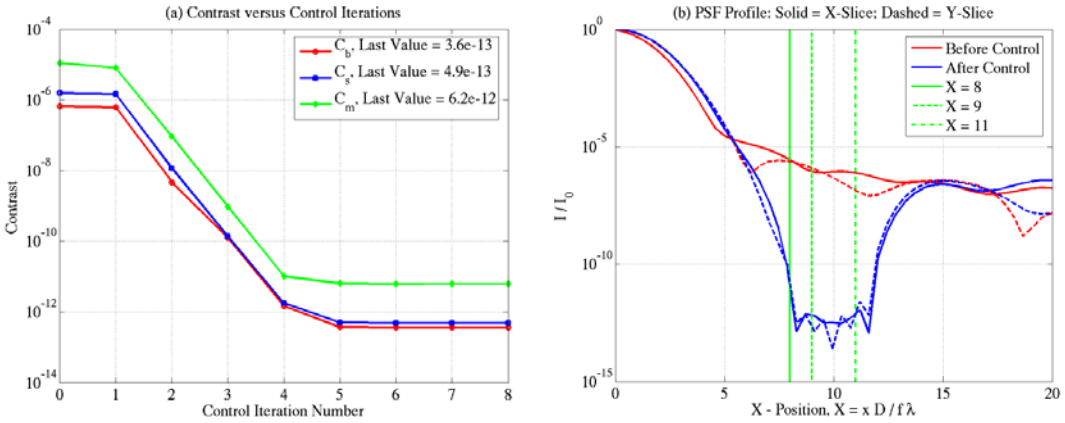

Figure 9. (a) Three types of contrast values versus control iteration number, where Iteration = 1 corresponds to the DMA tip/tilt control step carried out with DM1. (b) PSF slices along the x-axis (solid-line) and the y-axis (dashed-line), respectively. In Part (b), $I = I(x, y)$ is the image intensity of the PSF, and I_0 is its peak value. For the Y-Slice of the PSF, the X and the x in the horizontal axis need to be replaced with Y and y, respectively. The errors included in this simulation are the same as in Fig. 8.

Table 1. Summary of the values of three types of contrast, C_b , C_c and C_m, obtained before and/or after wavefront control when introducing different types of errors into the PIAA/HCIT system.

Case #	Error Source	Error Value	Remarks	C_b	C_s	C_m
1	Nominal		Before Control	9.4E-14	1.5E-12	1.1E-11
2	Figure Error	10 nm RMS	Before Control	2.5E-06	5.9E-06	3.4E-05
			After Control	1.4E-12	1.9E-12	2.5E-11
3	OAP2	R_x = 20 μrad	Before Control	7.5E-13	5.4E-10	1.5E-08
			After Control	9.4E-15	2.2E-14	1.7E-13
4	OAP2	R_y = 20 μrad	Before Control	6.4E-13	4.9E-10	1.4E-08
			After Control	8.3E-15	2.5E-14	1.9E-13
5	OAP2	R_z = 150 μrad	Before Control	5.2E-13	4.1E-10	1.1E-08
			After Control	8.4E-15	2.5E-14	1.8E-13
6	OAP2	T_x = 20 μm	Before Control	1.3E-12	8.7E-10	2.5E-08
			After Control	8.2E-15	2.4E-14	2.0E-13
7	OAP2	T_y = 20 μm	Before Control	1.3E-12	8.7E-10	2.5E-08
			After Control	1.8E-12	4.3E-11	4.9E-10
8	OAP2	T_z = 200 μm	Before Control	9.4E-14	4.3E-11	4.9E-10
9	Figure & OAP2 RB Errors	Fig. = 5nm RMS	Before Control	6.6E-07	1.6E-06	1.1E-05
		T_x = 5 μm	After Control	3.5E-13	4.9E-13	6.2E-12
10	OAP2 Focus	35 nm RMS	Before Control	1.3E-13	3.6E-12	2.4E-11
			After Control	1.7E-14	1.0E-13	3.1E-13
11	Fig=10nm RMS & STOP Tx or Ty	Tx = 3mm	After Control	1.5E-12	2.3E-12	2.2E-11
		Ty = 0.5μm	After Control	1.7E-12	2.8E-12	2.4E-11
12	DM1 Rotation	1 deg.	After Control	1.8E-12	3.7E-13	1.5E-11
		2 deg.	After Control	2.9E-09	5.9E-09	5.4E-08

4.3 Combination of Figure and OAP RB Errors

In this example, we examined a case in which the two types of errors investigated in two previous sub-sections are combined. For the figure error, we included all of the surface errors in Fig. 3 except that they are reduced by a factor of 2. For the RB error, we introduced $R_x = 5\,\mu\text{rad}$ into OAP2. The results are shown in Figures 8 and 9 and are summarized in Case 9 of Table 1. The 2-step WFC process works well in this case as well.

4.4 OAP Focus Error

We examined the impact of OAP focus error on the various contrast values by introducing 35nm RMS focus into OAP2. The results are shown in Figs. 10(a-e) as well as in Case 10 of Table 1. Figures 10(a-b) are the PSFs before and after WFC, Figs. 10(c-d) are the maps of the total DM strokes used, and Fig. 10(e) shows the PSF profiles before and after control. All three contrast values are worsened as compared to the error-free case (Case 1 in Table 1), but they can be improved to values better than the nominal case by WFC. In this case one only needs the DMA figure control step for the WFC.

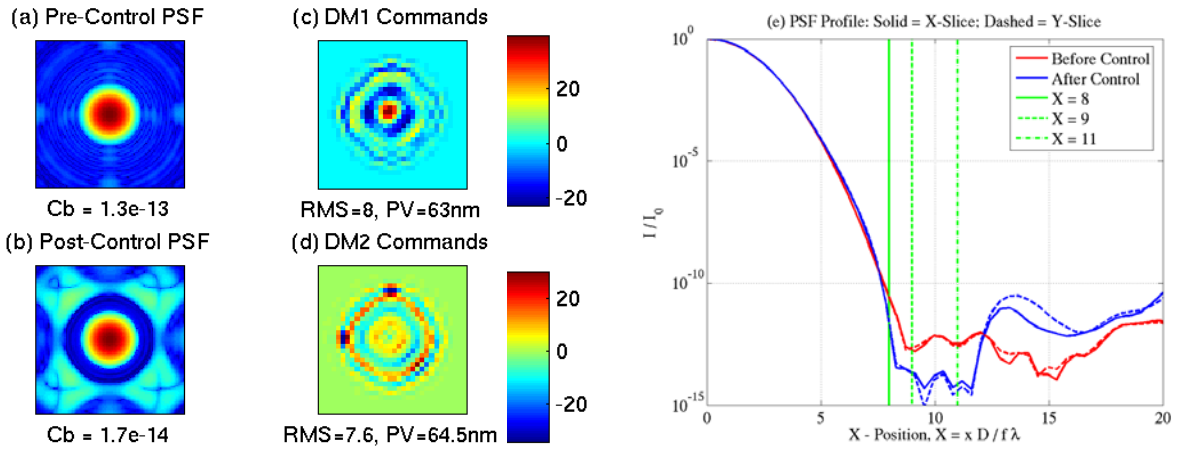

Figure 10. Parts (a)-(b) are the pre- and the post-control PSF maps plotted in a log-scale with a color-map stretch = 1E-15 – 1E0 inside the central $40\lambda/D \times 40\lambda/D$ region, and parts (c)-(d) the total DM stroke values in nm. Part (e) shows the PSF slices along the x-axis (solid-line) and the y-axis (dashed-line), respectively. The error included in this simulation is the 35nm RMS focus error of OAP2. Only the DMA figure control step is applied in this simulation.

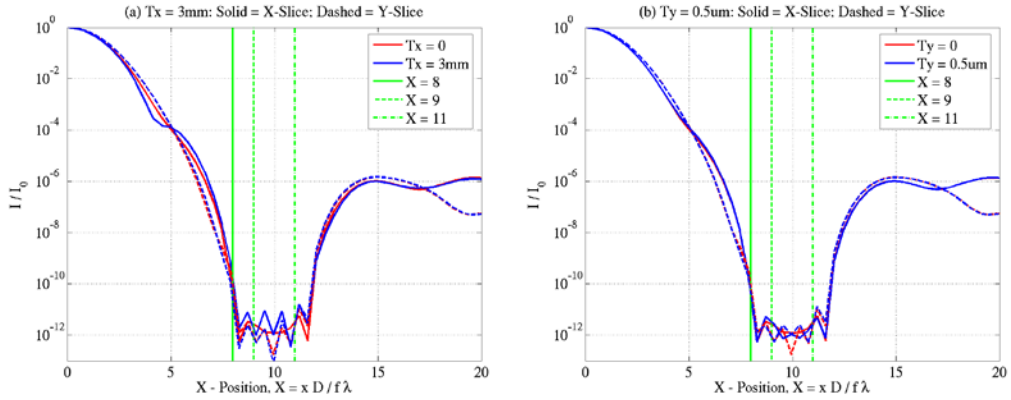

Figure 11. PSF slices along the x-axis (solid-line) and the y-axis (dashed-line), respectively. The errors included are the figure errors described in Fig.3 plus $T_x = 3\text{mm}$ in part (a) and $T_y = 0.5\,\mu\text{m}$ in part (b) for STOP, respectively. Only the DMA figure control step is applied in this simulation.

4.5 STOP Translation Error

In order to understand the effect of STOP translation error on the PIAA/HCIT's high-contrast performance, we investigated two cases where the STOP is translated in the direction of the x- and the y-axis, respectively, in addition to the figure errors treated in sub-section 4.1. The final PSF profiles of these two cases are compared in Figs. 11(a-b) with those obtained when the STOP is not translated, and the corresponding contrast results are summarized in Case 11 of Table 1. We found the DMA figure control process works fine for a fairly large value of STOP T_x, such as $T_x = 3\text{mm}$ in Fig. 11(a), but it does not work when the STOP translation in the y-direction, T_y, exceeds some small value, say, for example, when $T_y \geq 1\,\mu\text{m}$. The results in Fig. 11(b) are obtained with $T_y = 0.5\,\mu\text{m}$. This behavior of the PIAA/HCIT is similar to the case where OAP2 is translated in the y-direction (sub-section 4.2), and its cause is currently still being finvestigated.

4.6 DM RB Errors

One needs to take a new set of DM actuator influence functions every time after an accidental or a deliberate change occurs in the optical hardware. Measuring the influence functions of an optical system such as the one in Fig. 1 is a fairly time-consuming process. For example, to obtain a new set of influence functions for the PIAA/HCIT system, one needs to measure the PSF for at least 1268 times by poking one actuator at a time. In order to gain some rough understanding about how much RB change can be tolerated on two DMs after a set of influence functions were measured, for the case of figure errors analyzed in sub-section 4.1, we rotated DM1 by 1 and 2 degrees in the local coordinates (where the axis of rotation is perpendicular to the mirror surface) first, respectively, and then carried out DMA figure control. The results are shown in Figs. 12(a-b), and the corresponding contrast values are summarized as Case 12 in Table 1. These results show that, while ~1 degree rotation of DM1 is acceptable, a z-rotation of ~2 degrees or above greatly reduces the WFC ability of this DM. Similar behavior can be expected from DM2 as well.

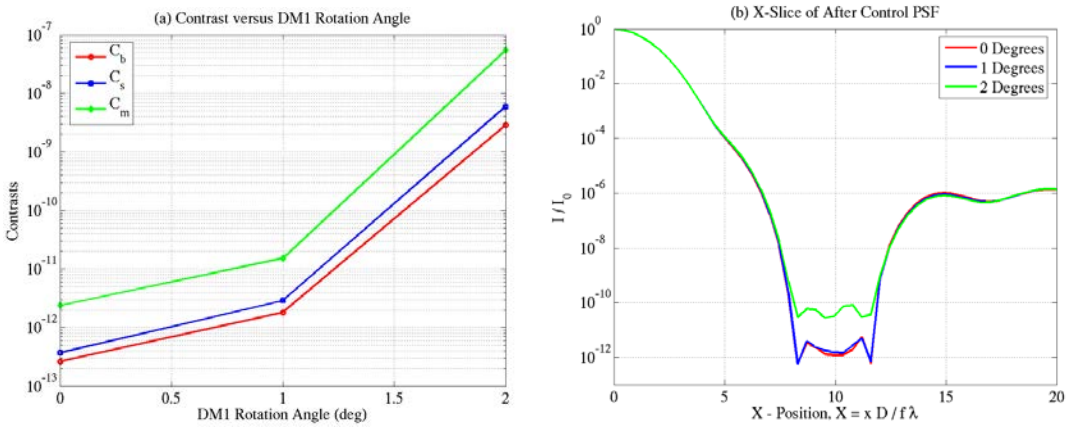

Figure 12. (a) Three contrast values as a function of DM1 rotation angle in the local coordinates. (b) Corresponding PSF slices along the x-axis. The errors included are the figure errors described in Fig.3. Only the DMA figure control step is applied in this simulation.

5. CONCLUSION

One of the key steps in the development of TPF Coronagraph is to validate each of its optical designs through modeling and error budget analysis. We have developed an optical simulation tool for the PIAA/HCIT hybrid system. This tool combines a ray trace, diffraction model, and a broadband wavefront control algorithm that operates directly on coronagraphic images, and is capable of performing full three-dimensional near-field diffraction analysis on HCIT's optical model. Using this tool, we have investigated the monochromatic light contrast performance sensitivity of the PIAA/HCIT system on the rigid-body and surface figure errors. We have shown that the degradation on the system contrast performance due to a variety of optical errors, such as rigid-body rotation and translation errors as well as surface figure errors, can be compensated through wavefront control using two sequential DMs. This study has been limited to a narrowband input light and a perfect PIAA unit. We plan to extend this work to broadband input light and imperfect mapping system in our future studies.

This work was carried out at the Jet Propulsion Laboratory, California Institute of Technology, under contract with the National Aeronautics and Space Administration.

REFERENCES

1. John T. Trauger, Chris Burrows, Brian Gordon, Joseph J. Green, Andrew E. Lowman, Dwight Moody, Albert F. Niessner, Fang Shi, and Daniel Wilson, "Coronagraph contrast demonstrations with the high-contrast imaging testbed," Proc. SPIE, **5487**, 1330, 2004.

2. Andrew E. Lowman, John T. Trauger, Brian Gordon, Joseph J. Green, Dwight Moody, Albert F. Niessner, and Fang Shi, "High-contrast imaging testbed for the Terrestrial Planet Finder coronagraph," Proc. SPIE, **5487**, 1246, 2004.
3. O. Guyon, "Phase-indueced amplitude apodization of telescope pupils fro extrasolar terrestrial planet imaging," A&A **404**, 379-387 (2003).
4. Stuart B. Shaklan and Joseph J. Green, "Reflectivity and optical surface height requirements in a broadband Coronagraph 1: Contrast floor due to controllable spatial frequencies," Appl. Opt. **45**, 5143-5153 (2006).
5. Stuart B. Shaklan, Joseph J. Green, and David M. Palacios, "The Terrestrial Planet Finder Coronagraph optical surface requirements," Proc. SPIE vol. **6265**, 62651I (2006).
6. M. G. Littman et al, "Phase and amplitude control ability using spatial light modulation and zero path length difference Michelson interferometer," Proc. SPIE **4854**, 405-412 (2003).
7. *Modeling and Analysis for Controlled Optical Systems User's Manual*, Jet Propulsion Laboratory, California Institute of Technology, Pasadena, CA.
8. Olivier Guyon, Subaru Telescope, NAOJ, 650 N. A'ohoku Pl., Hilo, HI 96720 (personal communications, 2008).
9. Erkin Sidick, Fang Shi, Scott Basinger, Dwight Moody, Andrew E. Lowman, Andreas C. Kuhnert, and John T. Trauger, "Performance of TPF's High-Contrast Imaging Testbed: Modeling and simulations, "Proc. SPIE, **6265**, 62653L, 2006.
10. Erkin Sidick, Scott A. Basinger, and David C. Redding, "An improved wavefront control algorithm for large space telescopes," Proc. SPIE, **7015**, 70154P (2008).
11. Amir Give'on *et al*, "Broadband wavefront correction algorithm for high-contrast imaging system," Proc. SPIE, **6691**, 66910A (2007).